Prolonged exposure to lung-derived cytokines is associated with activation of microglia in patients with COVID-19

Rogan A. Grant,[1] Taylor A. Poor,[1] Lango Sichizya,[1] Estefani Diaz,[1] Joseph I. Bailey,[1] Sahil Soni,[1] Karolina J. Senkow,[1] Xóchitl G. Pérez-Leonor,[1] Hiam Abdala-Valencia,[1] Ziyan Lu,[1] Helen K. Donnelly,[1] Lacy M. Simons,[2,3] Egon A. Ozer,[2,3] Robert M. Tighe,[4] Jon W. Lomasney,[5] Richard G. Wunderink,[1] Benjamin D. Singer,[1,6] Alexander V. Misharin,[1] and G.R. Scott Budinger,[1] for The Northwestern University Successful Clinical Response In Pneumonia Therapy (NU SCRIPT) Investigators[7]

[1]Division of Pulmonary and Critical Care Medicine, Department of Medicine; and [2]Division of Infectious Diseases, Department of Medicine, Feinberg School of Medicine, Northwestern University, Chicago, Illinois, USA. [3]Center for Pathogen Genomics and Microbial Evolution, Robert J. Havey, MD Institute for Global Health, Feinberg School of Medicine, Northwestern University, Chicago, Illinois, USA. [4]Division of Pulmonary, Allergy, and Critical Care Medicine, Duke University School of Medicine, Duke University, Durham, North Carolina, USA. [5]Department of Pathology, [6]Department of Biochemistry and Molecular Genetics, and Department of Medicine, Feinberg School of Medicine, Northwestern University, Chicago, Illinois, USA. [7]The NU SCRIPT Investigators are detailed in Supplemental Acknowledgments.

BACKGROUND. Survivors of pneumonia, including SARS-CoV-2 pneumonia, are at increased risk for cognitive dysfunction and dementia. In rodent models, cognitive dysfunction following pneumonia has been linked to the systemic release of lung-derived pro-inflammatory cytokines. Microglia are poised to respond to inflammatory signals from the circulation, and their dysfunction has been linked to cognitive impairment in murine models of dementia and in humans.

METHODS. We measured levels of 55 cytokines and chemokines in bronchoalveolar lavage fluid and plasma from 341 patients with respiratory failure and 13 healthy controls, including 93 unvaccinated patients with COVID-19 and 203 patients with other causes of pneumonia. We used flow cytometry to sort neuroimmune cells from postmortem brain tissue from 5 patients who died from COVID-19 and 3 patients who died from other causes for single-cell RNA-sequencing.

RESULTS. Microglia from patients with COVID-19 exhibited a transcriptomic signature suggestive of their activation by circulating pro-inflammatory cytokines. Peak levels of pro-inflammatory cytokines were similar in patients with pneumonia irrespective of etiology, but cumulative cytokine exposure was higher in patients with COVID-19. Treatment with corticosteroids reduced expression of COVID-19–specific cytokines.

CONCLUSION. Prolonged lung inflammation results in sustained elevations in circulating cytokines in patients with SARS-CoV-2 pneumonia compared with those with pneumonia secondary to other pathogens. Microglia from patients with COVID-19 exhibit transcriptional responses to inflammatory cytokines. These findings support data from rodent models causally linking systemic inflammation with cognitive dysfunction in pneumonia and support further investigation into the role of microglia in pneumonia-related cognitive dysfunction.

FUNDING. SCRIPT U19AI135964, UL1TR001422, P01AG049665, P01HL154998, R01HL149883, R01LM013337, R01HL153122, R01HL147290, R01HL147575, R01HL158139, R01ES034350, R01ES027574, I01CX001777, U01TR003528, R21AG075423, T32AG020506, F31AG071225, T32HL076139.

Authorship note: RAG and TAP contributed equally to this work as co–first authors. RGW, BDS, AVM, and GRSB contributed equally to this work and are co–corresponding authors.

Conflict of interest: BDS holds US patent 10,905,706, "Compositions and methods to accelerate resolution of acute lung inflammation," and serves on the scientific advisory board of Zoe Biosciences, in which he holds stock options.

Submitted: December 27, 2023
Accepted: March 13, 2024
Published: March 19, 2024

Reference information: *JCI Insight*. 2024;9(8):e178859. https://doi.org/10.1172/jci.insight.178859.

Introduction

Nearly 800 million people have been diagnosed with COVID-19, and 7 million people have died. In the United States alone, there are currently more than 100 million survivors of COVID-19 (1). Symptoms of post-acute sequelae of COVID-19 (PASC) are dominated by neurological, cognitive, and psychiatric dysfunction (2–5).

Cognitive impairment appears to be particularly common and long-lasting. A meta-analysis of world health records estimated that 2% of all symptomatic SARS-CoV-2 infections result in at least short-term cognitive impairment, with more than 50% of patients presenting to PASC centers reporting psychiatric symptoms and 15% of patients with PASC reporting sustained symptoms 1 year after initial infection (6). An increased risk of dementia persists for at least 2 years after severe COVID-19 (3), similar to what is observed following pneumonia secondary to other pathogens (7–9). These complications are more common in patients requiring intensive care unit (ICU) admission (10, 11).

Investigators have proposed several mechanisms to explain the cognitive dysfunction after COVID-19, many of which are specific to SARS-CoV-2 (12–22). Nevertheless, prolonged cognitive dysfunction in survivors of pneumonia or sepsis was recognized before the pandemic (4, 7–9, 23–26). In rodent models, circulating inflammatory cytokines enter the CNS and are sufficient to induce cognitive dysfunction (25, 27–32). These findings suggest that cognitive decline in pneumonia survivors might result from exposure to lung-derived inflammatory cytokines independent of the infecting pathogen. In support of this hypothesis, rigorous studies of clinical samples and autopsy tissues from patients who died from COVID-19 reveal that SARS-CoV-2 infection is limited to the lung epithelium and alveolar macrophages, and reliable evidence of direct infection of the CNS by SARS-CoV-2 is absent (7, 12, 14, 33–35). Indeed, careful studies of the mechanisms underlying the loss of taste and smell in patients with COVID-19 failed to find evidence of infection in olfactory neurons, instead implicating inflammatory signals from adjacent infected nasopharyngeal epithelia (14, 35).

Microglia are the most abundant immune cell population in the CNS. As such, they are poised to respond to inflammatory signals originating from the circulation. Furthermore, a wealth of evidence links dysfunction in microglia to cognitive dysfunction in rodent models and in humans (36–41). We and others have reported that the duration of illness in patients with severe SARS-CoV-2 pneumonia is much longer than in patients with pneumonia secondary to other pathogens (33, 42–47). We found this is driven, in part, by pro-inflammatory circuits between infected alveolar macrophages and T cells recruited into the lung (33). We reasoned that if CNS damage resulting from COVID-19 is the consequence of prolonged exposure to circulating pro-inflammatory cytokines, microglia from patients with COVID-19 would exhibit a transcriptional signature of cytokine-mediated activation (42).

Results

COVID-19 is associated with a transcriptional signature in microglia suggestive of NF-κB activation and cell cycle arrest. We collected frontal lobe samples at autopsy from 5 patients who died following SARS-CoV-2 infection and 3 patients who died without respiratory failure or sepsis between March 2021 and April 2022. Clinical features of these patients are included in Supplemental Table 1; supplemental material available online with this article; https://doi.org/10.1172/jci.insight.178859DS1. We generated single-cell suspensions of these tissues and enriched them for live microglia, T cells, and other neuroimmune cells using flow cytometry sorting (Supplemental Figure 1A). We then performed single-cell RNA-sequencing (scRNA-Seq) on these samples, identifying 65,767 cell passing quality control, predominantly heterogeneous populations of microglia and $CD8^+$ T cells (Figure 1, A–C). Cluster markers are listed in Supplemental Data 1.

We did not detect a single read of any SARS-CoV-2 gene or the negative-sense genome scaffold required for replication (48) when we aligned our scRNA-Seq reads to a hybrid genome containing the human GRCh38.93 genome build and the wild-type ancestral SARS-CoV-2 strain (NC045512.2) (Supplemental Figure 1B). Investigators have also suggested that PASC may result from Epstein-Barr virus (EBV) reactivation (49). However, we did not detect a single read of any EBV1 gene when we included a linearized EBV1 genome (NC007605.1) in our hybrid genome (Supplemental Figure 1C).

The development and progression of dementia have been associated with the accumulation of microglia with a distinct transcriptional phenotype defined by the expression of genes including *Apoe*, *Spp1*, *Lpl*, and *Cst7* in mice and *APOE*, *SPP1*, *CD81*, and *APOC1* in humans, which are called disease-associated microglia (DAMs) or Alzheimer's disease microglia, though similar states have also been observed during normal aging (38, 50, 51). We observed a population of DAM-like microglia in all patients, indicative of the advanced age of and history of neuropathology in some patients (Supplemental Table 1). Indeed, the fraction of microglia expressing a DAM phenotype was highest in a patient in the cohort without COVID-19 who had an antemortem diagnosis of dementia. The relative abundance of this microglial state was indistinguishable between groups (Figure 1B).

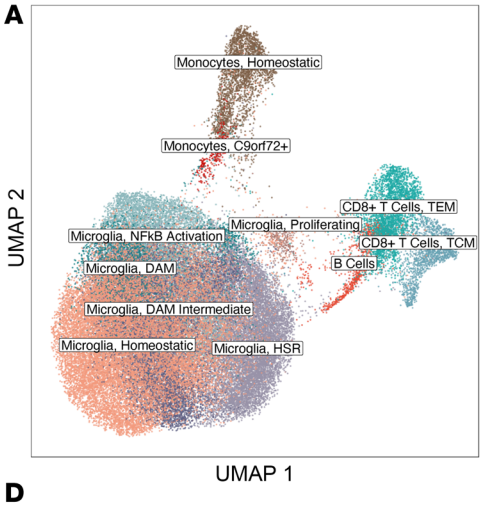
A
Monocytes, Homeostatic
Monocytes, C9orf72+
CD8+ T Cells, TEM
Microglia, Proliferating
Microglia, NFkB Activation
CD8+ T Cells, TCM
B Cells
Microglia, DAM
Microglia, DAM Intermediate
Microglia, Homeostatic
Microglia, HSR
UMAP 2
UMAP 1

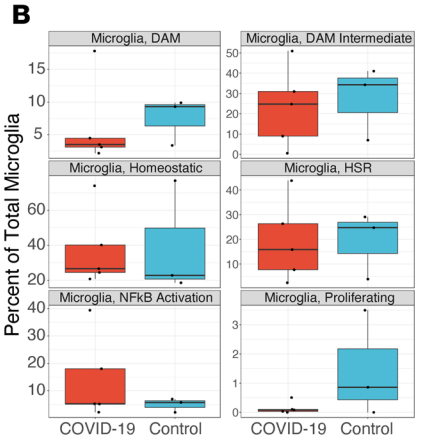
B
Microglia, DAM
Microglia, DAM Intermediate
Microglia, Homeostatic
Microglia, HSR
Microglia, NFkB Activation
Microglia, Proliferating
Percent of Total Microglia
COVID-19
Control

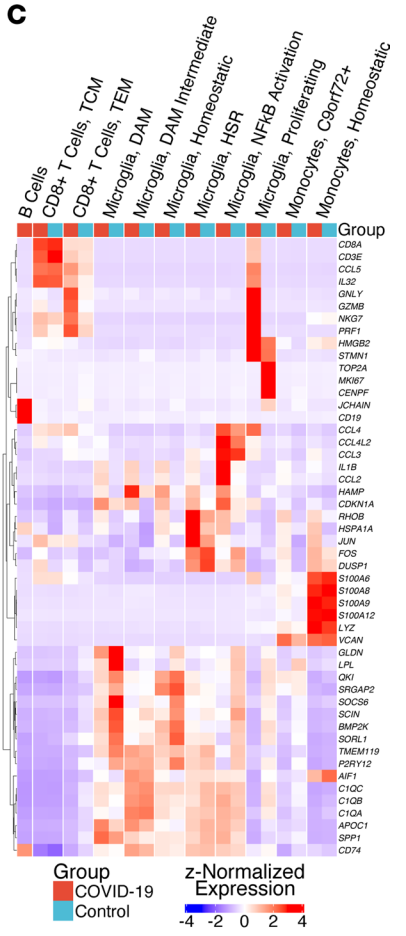
C
B Cells
CD8+ T Cells, TCM
CD8+ T Cells, TEM
Microglia, DAM
Microglia, DAM Intermediate
Microglia, Homeostatic
Microglia, HSR
Microglia, NFkB Activation
Microglia, Proliferating
Monocytes, C9orf72+
Monocytes, Homeostatic
Group
CD8A
CD3E
CCL5
IL32
GNLY
GZMB
NKG7
PRF1
HMGB2
STMN1
TOP2A
MKI67
CENPF
JCHAIN
CD19
CCL4
CCL4L2
CCL3
IL1B
CCL2
HAMP
CDKN1A
RHOB
HSPA1A
JUN
FOS
DUSP1
S100A6
S100A8
S100A9
S100A12
LYZ
VCAN
GLDN
LPL
QKI
SRGAP2
SOCS6
SCIN
BMP2K
SORL1
TMEM119
P2RY12
AIF1
C1QC
C1QB
C1QA
APOC1
SPP1
CD74
Group
COVID-19
Control
z-Normalized Expression
-4 -2 0 2 4

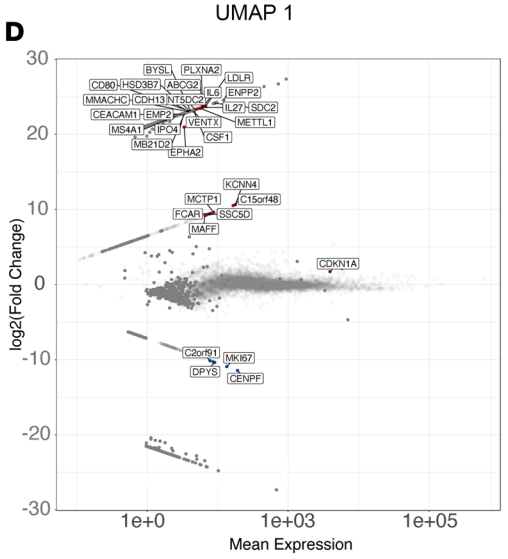
D
BYSL
PLXNA2
LDLR
CD80
HSD3B7
ABCG2
IL6
ENPP2
MMACHC
CDH13
NT5DC2
IL27
SDC2
CEACAM1
EMP2
VENTX
METTL1
MS4A1
IPO4
CSF1
MB21D2
EPHA2
KCNN4
MCTP1
C15orf48
FCAR
SSC5D
MAFF
CDKN1A
C2orf91
MKI67
DPYS
CENPF
log2(Fold Change)
Mean Expression

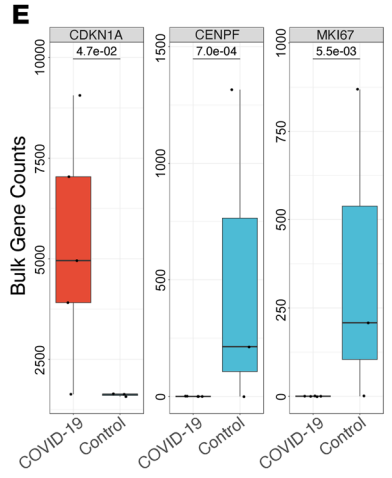
E
CDKN1A
4.7e-02
CENPF
7.0e-04
MKI67
5.5e-03
Bulk Gene Counts
COVID-19
Control

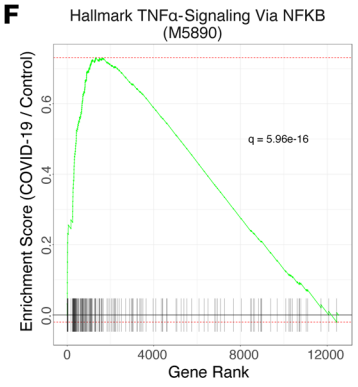
F
Hallmark TNFα-Signaling Via NFKB
(M5890)
q = 5.96e-16
Enrichment Score (COVID-19 / Control)
Gene Rank

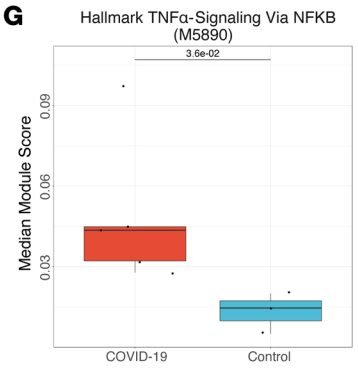
G
Hallmark TNFα-Signaling Via NFKB
(M5890)
3.6e-02
Median Module Score
COVID-19
Control

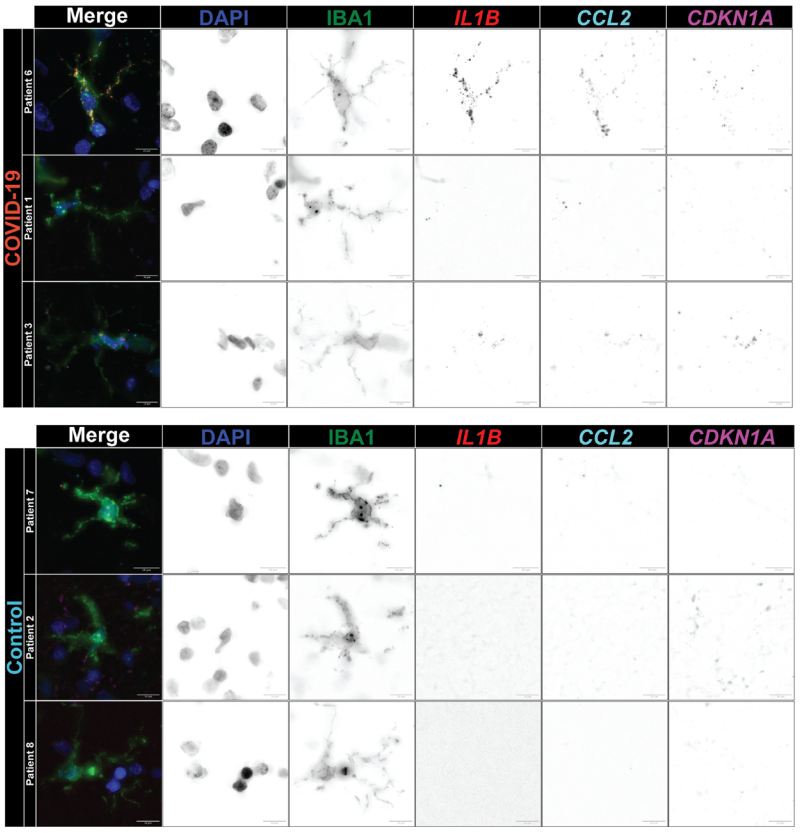
H
Merge
DAPI
IBA1
IL1B
CCL2
CDKN1A
COVID-19
Patient 6
Patient 1
Patient 3
Control
Patient 7
Patient 2
Patient 8

Figure 1. Microglia exhibit distinct transcriptional responses in patients with COVID-19. (**A**) Uniform manifold approximation and projection (UMAP) of 65,767 cells isolated from the frontal lobes of 8 patients postmortem. HSR, heat shock response; TCM, T central memory; TEM, T effector memory. (**B**) Relative abundance of microglial cell states as a percentage of total microglia. No significant differences are observed by diagnosis ($q \leq 0.05$, Mann-Whitney). (**C**) Hierarchical clustering of mean marker gene expression by cell type and cell state by diagnosis. (**D**) MA plot of differentially expressed genes in total microglia in COVID-19 versus controls by pseudobulk differential expression analysis. Significantly upregulated genes are shown in red, and significantly downregulated genes are shown in blue ($q < 0.05$, Wald test). Genes shown in gray are not significantly differentially expressed. (**E**) Callouts of key markers of cell division and cell cycle arrest from **D**. All genes shown are significantly differentially expressed ($q < 0.05$, Wald test). (**F**) Gene set enrichment of Hallmark TNF-α Signaling Via NF-κB (M5890) from pseudobulk differential expression analysis ($q = 5.96 \times 10^{-16}$, multilevel splitting Monte Carlo). (**G**) Median modular expression of Hallmark TNF-α Signaling Via NF-κB (M5890) by diagnosis. Points represent median expression in total microglia from each patient ($q = 2.6 \times 10^{-2}$, Mann-Whitney). (**H**) Representative images of combined immunofluorescence and smFISH (RNAScope) from human frontal lobe tissue sections showing cell cycle–arrested, pro-inflammatory microglia in patients with COVID-19 relative to controls. Images are pseudocolored by channel as follows: DAPI: blue, IBA1: green, *IL1B*: red, *CCL2*: cyan, *CDKN1A*: magenta.

To determine whether microglia from patients with COVID-19 exhibited a transcriptional signature distinct from patients who died from other causes, we performed pseudobulk differential expression analysis (DEA) on each major cell type cluster. This analysis revealed a pattern of gene expression in microglia from patients with COVID-19 that included a nearly complete downregulation of genes associated with cellular proliferation (*MKI67*, *CENPF*) and upregulation of the cell cycle arrest marker *CDKN1A* (encoding p21). Although this pattern of gene expression has been referred to as immunosenescence, it can also be seen in response to inflammation, and we did not detect significant upregulation of other senescence-associated genes (e.g., *CDKN2A*/p16 or *SERPINE1*/PAI-1; Figure 1, D and E). Complete DEA results are listed in Supplemental Data 2.

Cytokine exposure has been suggested to drive the long-lasting cognitive impairment resulting from severe pneumonia caused by other pathogens that lack neurotropism, including influenza A viruses and bacteria (4, 7–9, 23, 24). Some of these cytokines, including TNF-α, IL-6, and IL-1β, can directly cross the blood-brain barrier and act on resident immune cells in the CNS, including microglia (27–29). We examined whether microglia isolated from patients who died after SARS-CoV-2 infection exhibited an elevated response to any of these cytokines by comparing gene set enrichment using Molecular Signatures Database (MSigDB) Hallmark annotations (52). Through groupwise gene set enrichment analysis (GSEA) on pseudobulk data, we found that Hallmark TNF-α Signaling Via NF-κB (M5890) was the most significantly enriched gene set among all Hallmark gene sets in MSigDB ($q = 6.0 \times 10^{-16}$; Figure 1F). We further found through patientwise gene module analysis that Hallmark TNF-α Signaling Via NF-κB (M5890) gene expression was significantly elevated in individuals who died after SARS-CoV-2 infection, suggesting that prolonged exposure to TNF-α or other NF-κB–activating cytokines may drive cell cycle arrest in these patients ($q = 3.6 \times 10^{-2}$, Mann-Whitney; Figure 1G). To verify existence of this cell state in situ, we applied single-molecule FISH (smFISH) (RNAScope) to brain sections from the same patients to determine whether *CDKN1A*, *CCL2*, and *IL1B* were coexpressed in ionized calcium-binding adapter molecule 1–positive ($IBA1^+$) microglia. We consistently observed cells coexpressing all 3 genes in $IBA1^+$ microglia in samples from patients who died with COVID-19 that were absent in control samples (Figure 1H).

COVID-19 is associated with greater cumulative systemic exposure to inflammatory cytokines compared with other causes of pneumonia. To determine if the transcriptomic changes in microglia we observed in patients who died after SARS-CoV-2 infection could have resulted from exposure to unusually high levels of inflammatory cytokines, we performed multiplexed profiling of 72 cytokines, 55 of which were of sufficient quality for downstream analysis (Supplemental Figure 2). We analyzed serial plasma and alveolar samples collected by bronchoalveolar lavage (BAL) from 354 patients. These samples included patients with respiratory failure requiring mechanical ventilation for SARS-CoV-2 pneumonia ($n = 93$), pneumonia secondary to bacterial or fungal pathogens ($n = 162$), pneumonia resulting from other respiratory viruses ($n = 41$), conditions requiring mechanical ventilation for reasons unrelated to pneumonia ($n = 45$), and healthy controls ($n = 13$). Samples collected from all patients with respiratory failure were collected as part of an observational cohort study; samples from healthy controls were collected before the COVID-19 pandemic.

Comprehensive demographic data from these cohorts are available in Supplemental Table 2. Findings from this cohort have been previously reported (33, 53, 54). Patients with severe SARS-CoV-2 pneumonia were similar to other groups of mechanically ventilated patients in age, sex, and severity of illness as measured by the mean daily Sequential Organ Failure Assessment (SOFA; $q \geq 0.05$, Mann-Whitney), Acute Physiology Score (APS; $q \geq 0.05$, Mann-Whitney), and mortality ($q \geq 0.05$; χ^2 test of proportions); however, patients with nonviral pneumonias ("Other Pneumonia") were older ($q = 2.6 \times 10^{-2}$, Mann-Whitney) and

had higher SOFA scores ($q = 1.3 \times 10^{-3}$, Mann-Whitney) and APS scores ($q = 4.3 \times 10^{-2}$, Mann-Whitney). Patients with SARS-CoV-2 pneumonia were more likely to self-describe as Hispanic or Latino than all other groups ($q < 0.05$, χ^2 test of proportions) and had higher BMIs ($q < 0.05$, Mann-Whitney) compared with the rest of the cohort. Despite similar severity of illness on presentation and hospital mortality rate, the duration of mechanical ventilation and ICU stay was 1.8- to 2.4-fold longer in patients with SARS-CoV-2 pneumonia compared with all other groups of mechanically ventilated patients ($q < 0.05$, Mann-Whitney; Supplemental Data 3). In accordance with our previous findings, analysis of BAL fluid samples collected from all patients other than healthy controls revealed an elevated percentage of lymphocytes from patients with COVID-19 relative to all other groups of mechanically ventilated patients ($q < 0.05$, Mann-Whitney; Supplemental Data 3). A total of 187 in the cohort had BAL samples collected within 48 hours of intubation (early). Severity of illness scores and mortality rates were similar in patients with early BAL samples compared with the entire cohort of mechanically ventilated patients ($q \geq 0.05$, Mann-Whitney and $q \geq 0.05$, χ^2 test of proportions, respectively; Supplemental Data 4).

We proposed a model in which the relatively long clinical course of patients with COVID-19 results from spatially restricted inflammatory circuits between alveolar macrophages harboring SARS-CoV-2 and activated T cells in the alveolar space (33, 42). This model has since been confirmed by other groups (55–58). Enhanced transcription of chemokines promoting chemotaxis of monocytes and T cells, including *CXCL10*, *CCL8*, and *CCL2*, by monocyte-derived alveolar macrophages infected with or harboring SARS-CoV-2 is key to this model. In support of this model, samples collected within 48 hours of intubation from patients with COVID-19 clustered distinctly from other patient groups, driven by CXCL10 and CCL8 in BAL samples and CXCL10 in plasma (Figure 2, A and B). Elevated concentrations of CCL2 and CCL8 were also observed in BAL samples from patients with COVID-19, relative to patients with pneumonia secondary to nonviral pathogens ($q < 0.05$, Mann-Whitney; Figure 2, C and D). Indeed, concentrations of CXCL10 were significantly higher in the first 48 hours of intubation in both BAL fluid and plasma from patients with COVID-19, relative to all other groups ($q < 0.05$, Mann-Whitney), and CXCL10 protein levels, alone, on initial BAL (AUROC = 0.88, $P = 1.8 \times 10^{-5}$) and plasma draw (AUROC = 0.83, $P = 1.1 \times 10^{-5}$) were highly predictive of COVID-19 status (Supplemental Figure 2, G and H). Levels of CCL2 and CCL8 in BAL fluid as well as CXCL10 in plasma samples collected during the first 48 hours of intubation were higher in patients with COVID-19 relative to all other groups, with the exception of patients with other viral pneumonias ($q < 0.05$, Mann-Whitney; Figure 2, C and D).

Arguing against an unusually severe inflammatory response or "cytokine storm" in patients with COVID-19, the concentrations of other BAL fluid cytokines in samples collected during the first 48 hours of intubation, including CXCL1, IFN-γ, IL-1β, IL-6, IL-8, and TNF-α, were higher in patients with pneumonia relative to healthy controls but were largely similar between groups of mechanically ventilated patients (complete comparisons are included in Supplemental Data 7). A similar pattern was observed in the plasma of patients with COVID-19 compared with patients with other causes of pneumonia and respiratory failure (Figure 2D) (21, 22). Consistent with previous findings, the concentrations of IL-1β, IL-6, and TNF-α were higher in all groups of mechanically ventilated patients compared with healthy controls (Figure 2, C and D) (21).

We wondered whether the roughly 2-fold increase in the duration of illness in patients with COVID-19 might result in a higher cumulative exposure to pro-inflammatory cytokines. As the peak levels of inflammatory cytokines did not differ between patients with COVID-19 compared with similarly ill patients with pneumonia secondary to other pathogens, cumulative exposure could only be higher if the levels of inflammatory cytokines did not normalize over the course of the illness. We therefore performed geometric integration of cytokine expression over the ICU course, yielding a single value corresponding to an estimate of cumulative exposure to a given cytokine during the ICU stay (Figure 3E). Strikingly, samples originating from patients with COVID-19 — particularly patients with unfavorable outcomes — clustered together and were defined by greater cumulative exposure to pro-inflammatory cytokines in both BAL fluid and plasma (Figure 3, A and B). Among the many cytokines with significantly greater cumulative exposure in COVID-19 were CXCL10, CCL8, CCL2, IL-6, and TNF-α (Figure 3, C and D; $q < 0.05$, Mann-Whitney).

Levels of T cell and monocyte chemoattractants are lower in patients with severe COVID-19 who receive corticosteroid treatment. Prior to publication of the RECOVERY Collaborative study demonstrating efficacy of dexamethasone treatment in patients with severe COVID-19 (59), there was clinical equipoise concerning the prescription of systemic corticosteroids as a therapy for these patients. We took advantage of the inconsistent use of corticosteroids before this trial to examine their effect on cytokine expression in BAL fluid and plasma.

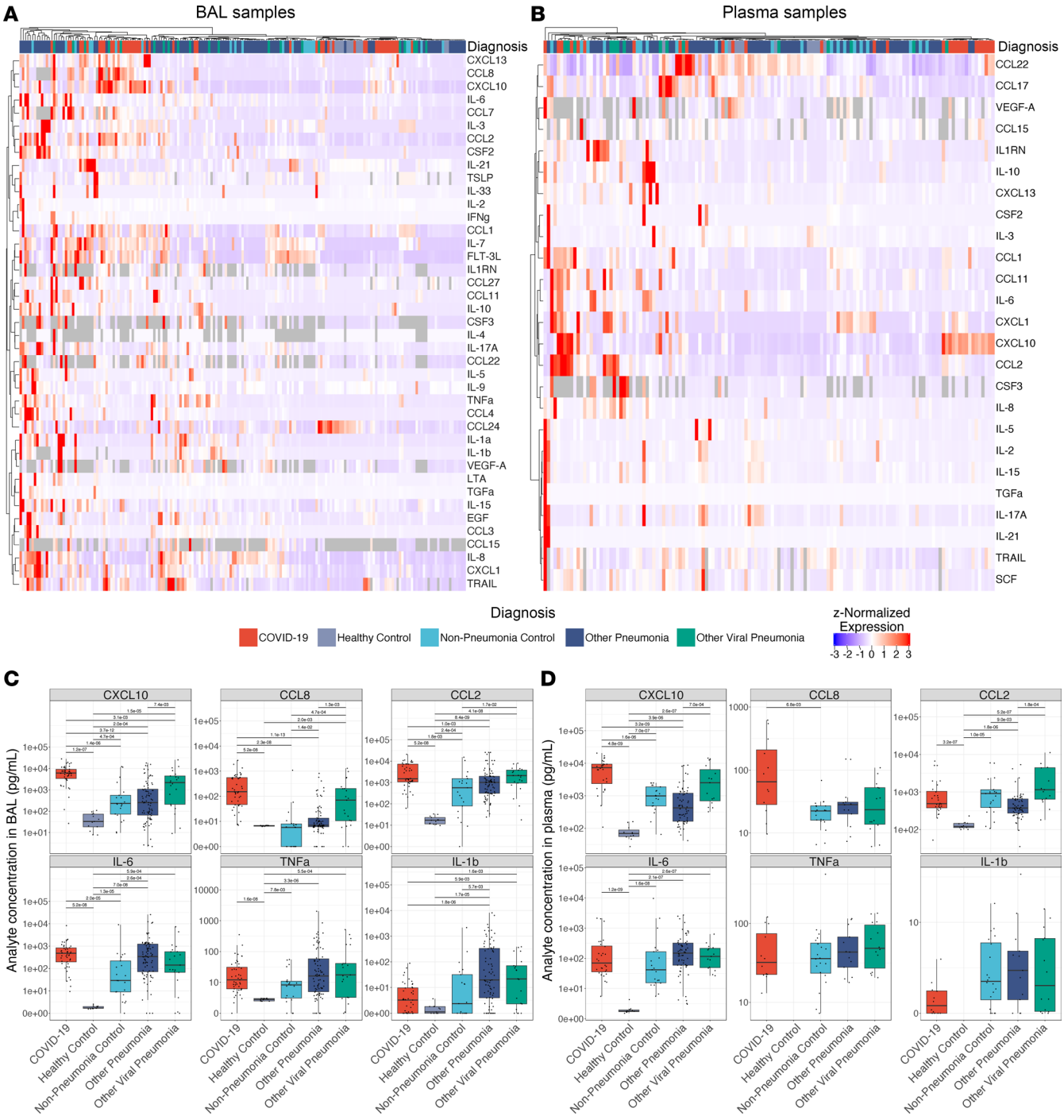

Figure 2. COVID-19 is distinguished from pneumonias of similar severity by expression of T cell and myeloid cell chemokines. (**A**) Hierarchical clustering of 41 cytokines showing significant variability by diagnosis ($q < 0.05$, Kruskal-Wallis) from 187 BAL samples collected in the first 48 hours of intubation from 183 patients with an early BAL. (**B**) Hierarchical clustering of 25 cytokines showing significant variability by diagnosis ($q < 0.05$, Kruskal-Wallis) from 137 early plasma samples from 134 patients. (**C**) Expression of COVID-19–defining T lymphocyte and monocyte chemokines and key pro-inflammatory cytokines from 479 BAL samples collected throughout the duration of mechanical ventilation from 332 patients. (**D**) Expression of COVID-19–defining T lymphocyte and monocyte chemokines and key pro-inflammatory cytokines from 396 plasma samples collected throughout the duration of mechanical ventilation from 262 patients.

We performed unbiased comparison of the concentrations of all 55 analytes as a function of steroid treatment. In BAL fluid, only the levels of CCL8, CXCL10, and CCL7 were significantly lower, and the levels of IL-10 were higher, in patients with COVID-19 after they received corticosteroids compared with those who did not receive corticosteroids ($q < 0.05$, Mann-Whitney). In plasma, only the concentrations of CXCL10 and

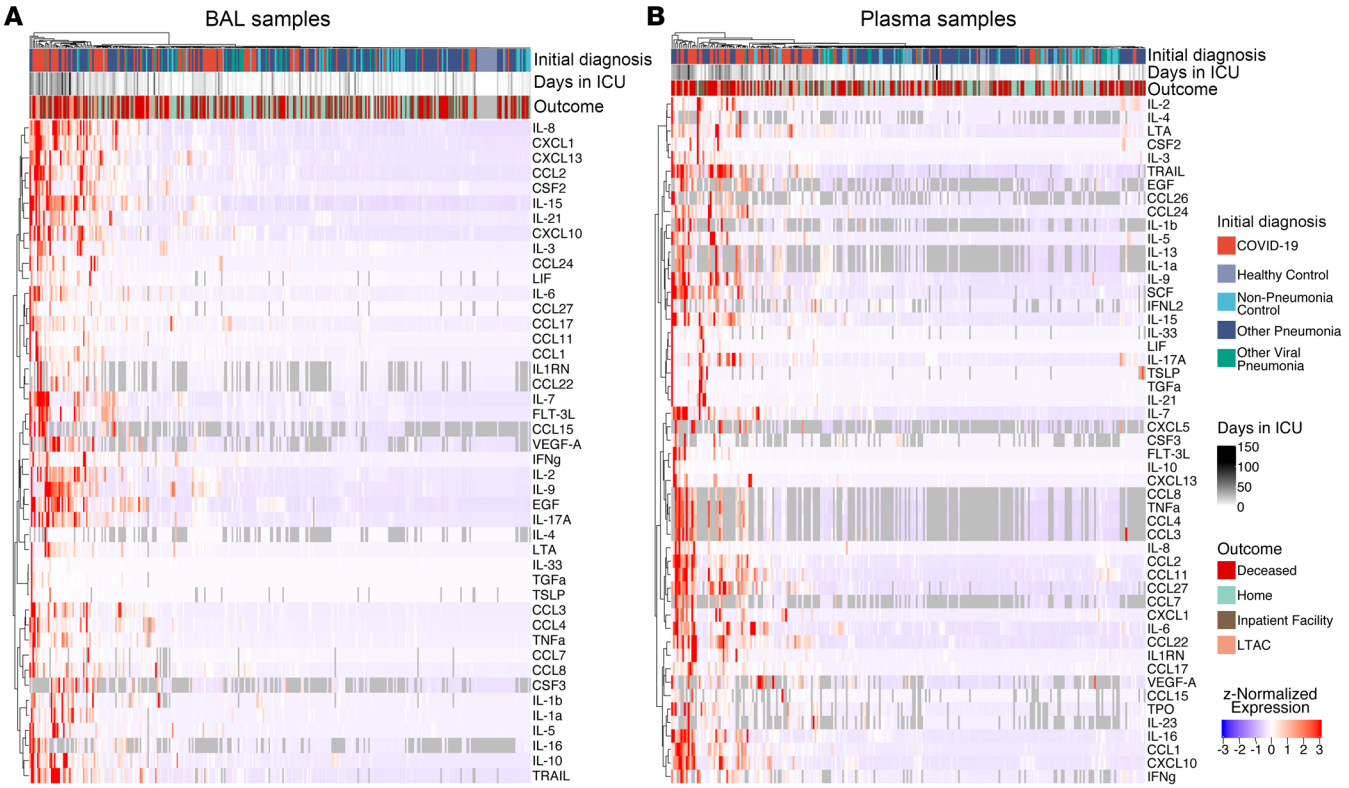
A
BAL samples
Initial diagnosis
Days in ICU
Outcome
IL-8
CXCL1
CXCL13
CCL2
CSF2
IL-15
IL-21
CXCL10
IL-3
CCL24
LIF
IL-6
CCL27
CCL17
CCL11
CCL1
IL1RN
CCL22
IL-7
FLT-3L
CCL15
VEGF-A
IFNg
IL-2
IL-9
EGF
IL-17A
IL-4
LTA
IL-33
TGFa
TSLP
CCL3
CCL4
TNFa
CCL7
CCL8
CSF3
IL-1b
IL-1a
IL-5
IL-16
IL-10
TRAIL
B
Plasma samples
Initial diagnosis
Days in ICU
Outcome
IL-2
IL-4
LTA
CSF2
IL-3
TRAIL
EGF
CCL26
CCL24
IL-1b
IL-5
IL-13
IL-1a
IL-9
SCF
IFNL2
IL-15
IL-33
LIF
IL-17A
TSLP
TGFa
IL-21
IL-7
CXCL5
CSF3
FLT-3L
IL-10
CXCL13
CCL8
TNFa
CCL4
CCL3
IL-8
CCL2
CCL11
CCL27
CCL7
CXCL1
IL-6
CCL22
IL1RN
CCL17
VEGF-A
CCL15
TPO
IL-23
IL-16
CCL1
CXCL10
IFNg
Initial diagnosis
COVID-19
Healthy Control
Non-Pneumonia Control
Other Pneumonia
Other Viral Pneumonia
Days in ICU
150
100
50
0
Outcome
Deceased
Home
Inpatient Facility
LTAC
z-Normalized Expression
-3 -2 -1 0 1 2 3

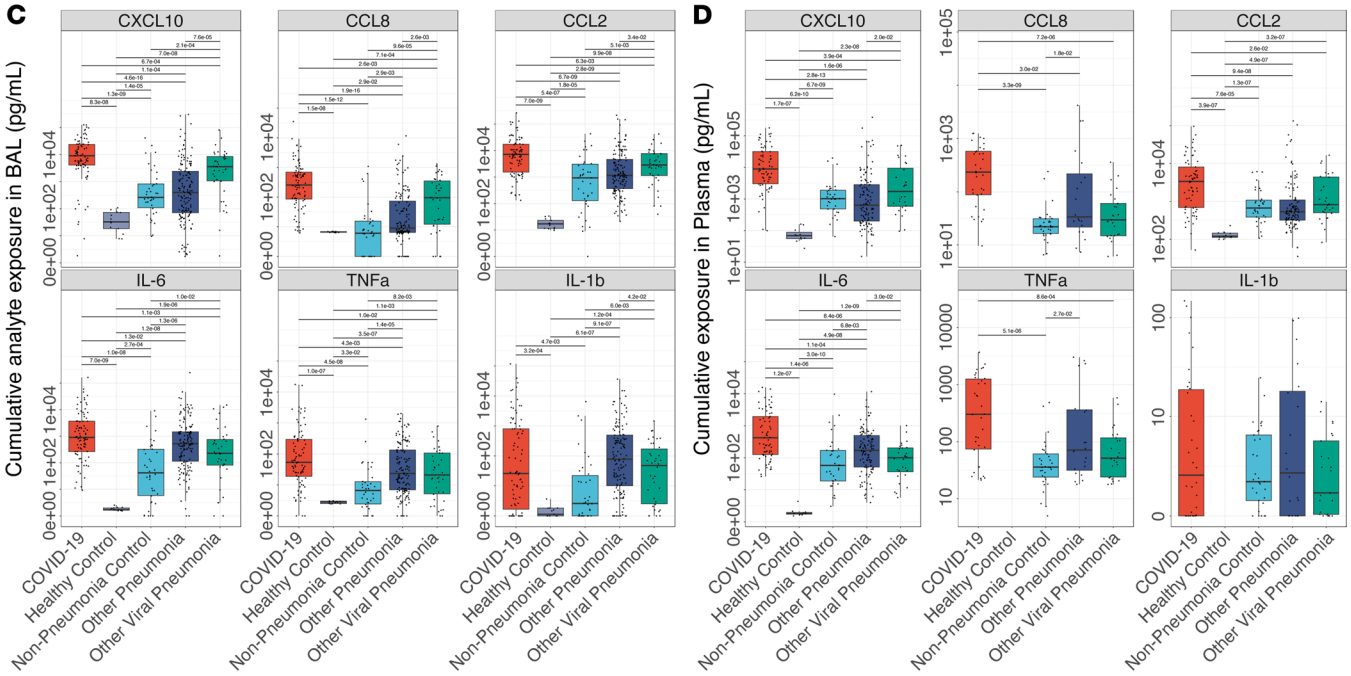
C
Cumulative analyte exposure in BAL (pg/mL)
CXCL10
CCL8
CCL2
IL-6
TNFa
IL-1b
0e+00 1e+02 1e+04
COVID-19
Healthy Control
Non-Pneumonia Control
Other Pneumonia
Other Viral Pneumonia
D
Cumulative exposure in Plasma (pg/mL)
CXCL10
CCL8
CCL2
IL-6
TNFa
IL-1b
0e+00 1e+02 1e+04
1e+01 1e+03 1e+05
10 100 1000 10000
0 10 100
COVID-19
Healthy Control
Non-Pneumonia Control
Other Pneumonia
Other Viral Pneumonia

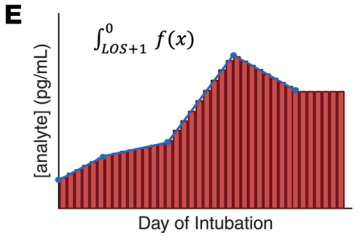
E
$\int_{LOS+1}^{0} f(x)$
[analyte] (pg/mL)
Day of Intubation

Figure 3. Cumulative but not peak exposure to pro-inflammatory cytokines is higher in patients with severe SARS-CoV-2 pneumonia compared with patients with severe pneumonia secondary to other pathogens. (**A**) Hierarchical clustering of cumulative exposure to 44 BAL cytokines showing significant variability by diagnosis ($q < 0.05$, Kruskal-Wallis) from 327 patients estimated by geometric integration of the levels of 479 BAL samples collected throughout the duration of mechanical ventilation. LTAC, long-term acute care. (**B**) Hierarchical clustering of cumulative exposure to 51 plasma cytokines showing significant variability by diagnosis ($q < 0.05$, Kruskal-Wallis) from 258 patients estimated by geometric integration of the levels of 396 plasma samples collected throughout the duration of mechanical ventilation. (**C**) Cumulative expression of selected pro-inflammatory cytokines in BAL fluid from **A**. (**D**) Cumulative expression of selected pro-inflammatory cytokines in plasma from **B**. (**E**) Schematic for calculation of cumulative exposure for each cytokine assayed for each patient throughout the course of mechanical ventilation by geometric integration. BAL samples from 3 patients and plasma samples from 2 patients receiving long-term mechanical ventilation were excluded from these analyses.

CCL7 were significantly lower, and IL-10 was significantly higher, after patients received corticosteroids ($q < 0.05$, Mann-Whitney). Notably, while these cytokines were detected in all groups of intubated patients, differences in the concentration of these cytokines as a function of corticosteroid treatment were only observed in patients with COVID-19 ($q \geq 0.05$, Mann-Whitney; Figure 4A), despite these patients receiving an equivalent hydrocortisone-equivalent dose of corticosteroids throughout their ICU stay as compared to similarly ill patient cohorts ($q \geq 0.05$, Mann-Whitney; Supplemental Figure 3). In previously published scRNA-Seq data of BAL fluid from this cohort, the expression of *CXCL10*, *CCL2*, *CCL7*, and *CCL8* was highest in monocyte-derived alveolar macrophages harboring SARS-CoV-2 (33).

Circulating cytokines in patients with COVID-19 originate from the alveolar space. We reasoned that if plasma cytokines in patients with SARS-CoV-2 originated from the alveolar space, we should observe a correlation between the concentration of BAL fluid cytokines and the concentration of plasma cytokines. When comparing all analytes for all paired BAL and plasma samples, we observed a significant, nonlinear correlation ($P = 0.49$, $P < 2.2 \times 10^{-16}$, Spearman rank correlation). Correlations were particularly strong for key cytokine markers of SARS-CoV-2 infection, including CXCL10 ($P = 0.55$, $q = 2.1 \times 10^{-25}$, Spearman rank correlation), CCL2 ($P = 0.52$, $q = 3.1 \times 10^{-22}$, Spearman rank correlation), CCL8 ($P = 0.41$, $q = 1.6 \times 10^{-5}$, Spearman rank correlation), and IL-6 ($P = 0.38$, $q = 5.3 \times 10^{-11}$, Spearman rank correlation). We also compared the concentrations of inflammatory cytokines in paired BAL fluid and plasma samples. Despite the 10- to 100-fold dilution of alveolar fluid by the BAL procedure (60), measured concentrations of many inflammatory cytokines in BAL fluid, including IL-6, IL-1β, CCL2, and CCL8, exceeded the concentrations in plasma, while the levels of CXCL10 and TNF-α were similar (Figure 4B). These data suggest the alveolus is the major contributor to pro-inflammatory cytokine levels in plasma during COVID-19 and are consistent with the known tropism of SARS-CoV-2 for the respiratory epithelium and alveolar macrophages (61).

We then used previously published scRNA-Seq data from BAL fluid obtained from 10 patients in this cohort to identify candidate cells in the lung that might be the source of inflammatory cytokines (33). Monocyte-derived alveolar macrophages expressed high levels of *CXCL10*, *CCL8*, *CCL2*, *CCL3*, and *IL1RN*. Surprisingly, while IL-6 concentrations were higher in BAL fluid from patients with COVID-19, and these concentrations were strongly correlated with plasma concentrations, we did not identify cells expressing *IL6* in BAL fluid, suggesting this cytokine is produced by cells in the lung parenchyma that are not sampled by the BAL procedure (Figure 4C).

Discussion

Neurologic and psychiatric symptoms are among the most common complaints in patients with PASC (2–5). Even more concerning, survivors of severe pneumonia, particularly the elderly, are at an increased risk of dementia for years after hospitalization (7–9). Although some studies have suggested these symptoms result from direct infection of the CNS by SARS-CoV-2, rigorous studies of clinical samples and autopsy tissues from patients who died from COVID-19 reveal that SARS-CoV-2 infection is limited to the airway epithelium and alveolar macrophages (5, 12, 13, 33, 62, 63). In instances when SARS-CoV-2 was detected in the brain, it was limited to the hypothalamus, which is anatomically adjacent to the nasopharynx and has a relatively permeable blood-brain barrier, raising the question of artifactual contamination during tissue processing (17). In flow cytometry–sorted immune cells from the cortex of a small cohort of patients who died after a diagnosis of COVID-19, we did not detect direct CNS infection with SARS-CoV-2 or reactivation of EBV1. Instead, we saw a transcriptional phenotype in microglia that included downregulation of genes associated with proliferation, upregulation of *CDKN1A*, and higher expression of inflammatory genes associated with signaling through TNF-α. Consistent with this finding, cumulative exposure to TNF-α and other cytokines originating from the lungs of patients with COVID-19 was higher relative to patients with

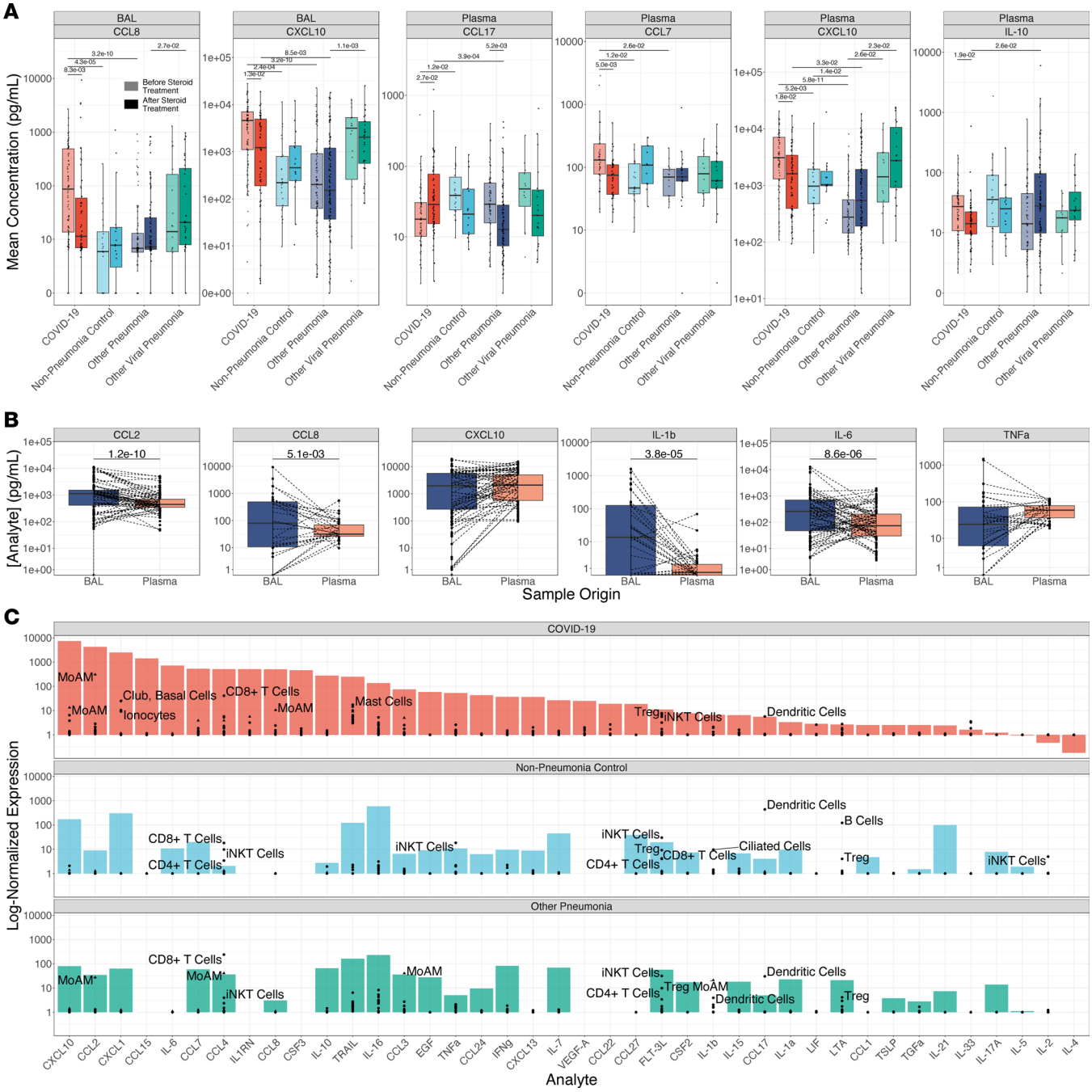

Figure 4. Corticosteroid treatment is associated with reductions in T cell and myeloid cell chemokine expression predominantly in monocyte-derived alveolar macrophages. (**A**) Box plots of cytokine expression for all BAL fluid and plasma cytokines exhibiting significantly altered expression ($q < 0.05$, Mann-Whitney) following corticosteroid treatment. Lightly shaded boxes represent cytokine expression values prior to corticosteroid treatment, and darkly shaded boxes represent expression values after corticosteroid treatment. (**B**) Paired comparisons of cytokine expression in BAL and plasma for all paired samples (paired Mann-Whitney). (**C**) Deconvolution of "bulk" cytokine expression in BAL fluid by scRNA-Seq of cells isolated from BAL fluid. Mean cytokine gene expression for each cell type detected in scRNA-Seq data (33) (black points) is overlaid on bulk cytokine expression by multiplexed cytokine array (filled bars) to identify cell type contributors to cytokine expression. MoAM, monocyte-derived alveolar macrophage; TRAM, tissue-resident alveolar macrophage; Treg, $CD4^+$ regulatory T cell; iNKT, invariant natural killer T cell.

pneumonia from other pathogens. As microglial inflammation has been demonstrated to reduce neuronal plasticity, synapse density, and memory formation (25, 26, 64–66), these changes may partly explain deficits in executive function observed in COVID-19 survivors (2, 10).

Whether the cognitive changes and increased rates of dementia observed in patients with COVID-19 are more severe or frequent than those observed in survivors of pneumonia secondary to

other pathogens is unknown (7–9). Consistent with another report, we found the levels of inflammatory cytokines originating in the lung at the time of peak illness severity (within 48 hours of intubation for respiratory failure) were similar in patients with COVID-19 compared with patients with pneumonia secondary to other pathogens (67). We took advantage of serial sampling in our cohort to show that the levels of lung-derived inflammatory cytokines remain elevated in patients with COVID-19 over the course of their ICU stay. As we and others have reported, the duration of critical illness is twice as long in patients with COVID-19 compared with patients with pneumonia secondary to other pathogens (33, 42–47). The data reported here show that patients with COVID-19 have a higher cumulative systemic exposure to lung-derived inflammatory cytokines during their illness and suggest a "cytokine monsoon" rather than "cytokine storm" might drive more severe or prolonged post-acute sequelae of infection in COVID-19 survivors through prolonged activation of NF-κB.

Using data obtained from the analysis of alveolar samples, we developed a model that explains the long duration of illness in patients with COVID-19, which has been confirmed by other groups (55–58) and has been suggested to contribute to downstream pathology even after apparent recovery (68). Key to this model is the presence of self-sustaining inflammatory circuits between alveolar macrophages harboring or infected with SARS-CoV-2 and activated T cells in the alveolar space that are maintained by the release of CXCL10, CCL8, and CCL2. Our findings support this model by showing alveolar and plasma levels of these cytokines differentiate patients with COVID-19 from patients infected with other pathogens. Moreover, we found that corticosteroids, which are effective in SARS-CoV-2 but are not universally effective in all causes of pneumonia, were associated with lower levels of these inflammatory cytokines in the lung and plasma, possibly by targeting their expression from alveolar macrophages harboring SARS-CoV-2 (59, 69).

Our study has limitations. Most importantly, while our sampling of alveolar fluid and plasma includes the largest cohort of patients reported to date, our analysis of cortical tissue includes only a single anatomical region, intentionally heavily enriched for microglia over other immune and non-immune cell populations, from a small group of patients in whom cytokine exposure was inferred rather than directly measured. These samples also originate from a cohort distinct from that used for cytokine measurements. It is therefore possible that microglial phenotypes that develop in a minority of patients were missed in our analysis or that our small cohort represents outliers. Additionally, other brain regions may demonstrate distinct patterns of resident immune cell activation. Second, while our data suggest the transcriptomic changes in microglia we observe in patients with COVID-19 are induced by TNF-α and other cytokines, we cannot infer causality from these observational data. As an alternative hypothesis, tissue hypoxia resulting from COVID-19–induced vascular injury could account for inflammatory activation of microglia through HIF-1α (31, 70–73), or cognitive dysfunction may result from other lung-derived damage-associated molecular patterns, neurotoxic agents, or pro-inflammatory molecules (74–76). Third, the administration of corticosteroids in our observational cohort was not randomized and did not include a placebo control. We therefore cannot conclude the differences in cytokine expression we observed are causally linked to steroid administration. Fourth, as our scRNA-Seq data from BAL fluid do not effectively capture all lung cell types, we cannot determine if alveolar macrophages are the primary contributors to the expression of chemokines that attract and activate T cells and monocytes. Finally, all samples were collected between March 2021 and April 2022, after which novel mutant strains of SARS-CoV-2 continued to arise. We therefore cannot determine whether our findings are directly applicable to SARS-CoV-2 strains dominant after April 2022.

Methods

Sex as a biological variable. Patients of both biological sexes were included in all arms of this study. Sex was not explicitly modeled as a biological variable because of limited statistical power.

Human participants (BAL and plasma collection). Patients at least 18 years of age with suspicion of pneumonia based on clinical criteria (including but not limited to fever, radiographic infiltrate, and respiratory secretions) were screened for enrollment into the SCRIPT study. Inability to safely obtain BAL or nonbronchoscopic BAL (NBBAL) were considered exclusion criteria (77). In our center, patients with respiratory failure are intubated based on the judgment of bedside clinicians for worsening hypoxemia, hypercapnia, or work of breathing refractory to high-flow oxygen or noninvasive ventilation modes. All patients were admitted to Northwestern Memorial Hospital in Chicago between June 15, 2018, and

September 29, 2021. Bronchoscopy was most commonly performed as part of routine clinical care to guide antimicrobial therapy, with paired blood draws for plasma for most samples. Procedures for patient care are outlined (33). Pneumonia category adjudication was performed by 5 critical care physicians using a published protocol (78). Clinical laboratory data were obtained from the Northwestern Medicine Enterprise Data Warehouse using Structured Query Language. APS and SOFA scores were generated from the electronic health record using previously validated programming. Anonymized clinical data from this cohort are available on Physionet (https://doi.org/10.13026/5phr-4r89) (53, 54). A complete list of the investigators involved in this study is available in Supplemental Data 5. Strain information for patients with COVID-19 is available in the Supplemental Data 6.

NBBAL and BAL procedures (Northwestern University). Consent was obtained from patients or legal decision makers for the bronchoscopic procedures. Bronchoscopic BAL was performed in intubated ICU patients with flexible, single-use Ambu aScope (Ambu) devices. Patients were given sedation and topical anesthetic at the physician proceduralist's discretion. Vital signs were monitored continuously throughout the procedure. The bronchoscope was wedged in the segment of interest based on available chest imaging or intraprocedure observations; aliquots of 30 cc of normal saline at a time, generally 90–120 cc total, were instilled and aspirated back. The fluid returned following the first aliquot was routinely discarded. Samples were split (if sufficient return volume was available) and sent for clinical studies, and an aliquot was reserved for research. A similar procedure was applied to NBBAL; however, NBBAL was performed with directional but not visual guidance and as usual procedural care by a respiratory therapist rather than a pulmonologist (77). In most cases the early bronchoscopy was performed immediately after intubation (77).

BAL procedures (Duke University healthy controls). Bronchoscopic BAL was performed in patients in the bronchoscopy suite or in the ICU. Patients were given sedation and topical anesthesia at the discretion of the physician performing the bronchoscopy. The most involved bronchopulmonary segment was identified based on clinician based on review of the chest CT scan, and 90–120 mL of saline was instilled into the segment of interest and aspirated back, with the first 5 cc of return discarded.

Plasma collection. Patient whole blood was collected in lithium heparin tubes on the same day BAL or NBBAL procedures were performed. The cellular fraction was spun down for 10 minutes at 1,690*g* at 4°C, and the plasma fraction was removed and stored at –80°C prior to multiplexed cytokine analysis.

Human brain autopsy. During routine brain autopsy, sections of the frontal cortex were removed by dissection and placed in sufficient precooled HypoThermosol solution (BioLife Solutions 101104) to cover. Postmortem interval for all samples is reported in Supplemental Table 1. Under aseptic conditions, any remaining arachnoid mater was removed on ice and discarded. Samples were then divided into 2 sections. The minor section was fixed in ice-cold fresh 4% formaldehyde (Electron Microscopy Sciences 15714) in 1× PBS for 48–72 hours, before being transferred to 1× PBS (Corning 21-040-CM) + 0.01% sodium azide (MilliporeSigma S2002) indefinitely. The major section was chopped into approximately 3 mm strips, stored at 4°C in HypoThermosol FRS (BioLife Solutions 101102), and processed for flow cytometry sorting as described below 0–48 hours later.

Human brain tissue processing and isolation of single-cell suspension. Free-floating sections were placed on ice and rinsed briefly with 1× HBSS (Thermo Fisher Scientific 21023CM) and strained. Tissues were then chopped thoroughly in 1 mL ice-cold digest buffer consisting of 1× Papain Dissociation System (Thermo Fisher Scientific NC9212788; 1 vial dissolved in 5 mL HBSS to yield 20 U of papain/mL in 1 mM L-cysteine with 0.5 mM EDTA) and 1 mg/mL DNase I (Roche 10104159001) with curved scissors. Chopped tissue was then transferred to gentleMACS C-tubes (Miltenyi Biotec 130-093-237) and mixed with 1 mL HBSS. Samples were then mechanically dissociated using a gentleMACS Octo Dissociator using the stock program "m_brain_03_01." Samples were then shaken at 200 rpm, 37°C, for 30 minutes, followed by a second round of mechanical dissociation. Digestion was then stopped by mixing samples with 18 mL ice-cold, sterile-filtered 1% BSA (MilliporeSigma SLBW2268) in 1× HBSS. Cell suspensions were then mashed through a 70 μm filter with 3 × 10 mL ice-cold 1% BSA in HBSS into a fresh 50 mL conical tube. The resulting single-cell suspension was then pelleted at 400*g* for 10 minutes at 4°C and resuspended in 25 mL RT 30% Percoll (MilliporeSigma GE17-0891-01) in 1× HBSS without calcium or magnesium (Gibco 14185-052). The resultant suspension was then slowly layered on top of 5 mL 70% Percoll in 1× HBSS without calcium or magnesium. Density centrifugation was performed at 600*g*, brake 0, and acceleration 4 for 30 minutes at room temperature (RT). Myelin and debris were removed using a vacuum apparatus, and 5–10 mL of the cell-containing interphase was transferred to a fresh 50 mL

conical tube, discarding the RBC/debris pellet. The purified cell suspension was then diluted 3:1 in ice-cold 1× HBSS and pelleted at 400*g* for 5 minutes at 4°C. Cells were then resuspended in 15 mL ice-cold 1× HBSS and again pelleted at 400*g* for 5 minutes at 4°C and resuspended in 500 μL ice-cold MACS buffer (Miltenyi Biotec 130-091-221). A 10 μL aliquot was then mixed with 10 μL 2× AOPI (Nexcelom NC1412892) and counted using a Cellometer K2. Remaining cells were then pelleted at 400*g* for 5 minutes at 4°C and resuspended at 1 × 10^6 cells/mL in ice-cold BamBanker medium (Bulldog Bio BB02). Cell suspensions were aliquoted at 2.5 × 10^5 to 5.0 × 10^5 cells and frozen directly at –80°C until sorting.

Cryorecovery and flow cytometry sorting of human microglia. Frozen human brain single-cell suspensions were thawed rapidly in a 37°C water bath with swirling and transferred to fresh 50 mL conical tubes. Cell suspensions were then diluted slowly with prewarmed RPMI 1640 (Thermo Fisher Scientific MT10041CV) + 5% FBS (Gibco 26140079), 50 μL every 5 seconds with agitation until 1.5 mL, 100 μL every 5 seconds with agitation until 5 mL total volume. The resultant suspension was then filtered through a 70 μm strainer and washed with 500 μL RPMI + 5% FBS and spun down at 400*g* for 10 minutes at RT. Cells were then resuspended in 50 μL ice-cold 1:10 human TruStain FcX (BioLegend 422302) in MACS buffer and incubated for at least 5 minutes on ice. A 2 μL aliquot was then counted on a Cellometer K2 as above. Samples were then mixed with 50 μL antibody cocktail/1 × 10^6 cells (minimum 50 μL; see cocktail below) and incubated at 4°C in the dark for 30 minutes. Cells were then diluted with 900 μL ice-cold MACS buffer and pelleted at 400*g* for 5 minutes at 4°C and resuspended in 400 μL ice-cold MACS buffer. Immediately before sorting, suspensions were filtered through a 70 μm filter and rinsed with 100–600 μL MACS buffer. SYTOX stain (Invitrogen S34860) was then added at 1 μL, and the suspension was mixed thoroughly. Cells were then sorted into PBS + 4% BSA (MilliporeSigma A1595-50ML) in DNA low-bind tubes (Eppendorf 022431005) using a FACSAria SORP (BD Biosciences) in a BioProtect IV-LE-Bio Containment Hood with a 100 μm nozzle. For scRNA-Seq, cells were sorted as singlet, nondebris, live ($SYTOX^-$), $CD56^-$, $CD15^-$, $CD45^+$, $HLA\text{-}DR^+$ events. Microglia were further subdivided as $(CD14/CD3/CD19)^-$ events for flow cytometry. Full antibody information is provided in Supplemental Table 3.

ScRNA-Seq. Sorted cells were diluted to 1.5 mL with BamBanker medium and immediately pelleted at 400*g* for 5 minutes at 4°C. Cells were then resuspended in PBS + 4% BSA at ~1 × 10^6 cells/mL. Cell concentrations and viability were confirmed using a Cellometer K2 as above. Libraries were then generated using the 10x Genomics 5' V2 kit, according to manufacturer's instructions (CG000331 Rev A), using a 10x Genomics Chromium Controller. After quality checks, scRNA-Seq libraries were pooled and sequenced on a NovaSeq 6000 instrument using an S1 flow cell (Illumina 20028319).

ScRNA-Seq analysis and processing. Data were processed using the Cell Ranger 7.0.1 pipeline (10x Genomics) with intronic reads disabled. To enable detection of viral RNA, reads were aligned to a custom hybrid genome containing GRCh38.93 and SARS-CoV-2 (NC_045512.2). An additional negative-strand transcript spanning the entirety of the SARS-CoV-2 genome was then added to the GTF and GFF files to enable detection of SARS-CoV-2 replication as described (33). Samples were genetically demultiplexed using the supplied "common_variants_grch38.vcf" reference, stripped of genetically defined doublet cells. Putative heterotypic doublets were then flagged for removal using scrublet 0.2.3 with manual thresholding of doublet scores, before removal using custom scripts in R (79). Detection and removal of empty droplets were then performed using cellbender 0.2.0 using GPU optimization with a 40 GB Tesla A100 GPU (80). Where applicable, expected cell numbers were determined using the 10x Genomics 5' V2 kit manual. Thresholding of initial filtering and preprocessing was performed using Seurat 4.2.1 (81), followed by integration using SCVI within SCVItools 0.14.3 (82), and reimported into Seurat for all clustering, dimensional reduction, and all downstream high-level analysis using built-in Seurat functions and custom scripts in R. All manipulations in Seurat were performed with the aid of tidyseurat 0.5.3 (83). Normalization was performed using SCTransform 0.3.5 (84), and clustering was performed using the Leiden algorithm. Default parameters were otherwise used unless directly specified (85). Cluster markers for Figure 1C were chosen as follows. First, the top 5 markers (as determined by average $\log_2$ fold-change) for each named cluster were identified in an unbiased manner using the FindAllMarkers() function in Seurat with only.pos set to TRUE. For readability, uninformative markers or methodological artifacts were manually removed, including genes matching the regular expression "-RP[LS]|-MT-|-EEF|-SH3," as well as *MALAT1*, *NEAT1*, *AHNAK*, *SNHG29*, *ITM2B*, *HMGN2*, *ARL6IP1*, *SYNE2*, and *APOC2*. The following genes were then manually included based on well-defined cell type and state markers as well as the results of the pseudobulk DEA: *AIF1*, *TMEM119*, *P2RY12*, *CD3E*, *CD8A*, *CD19*, *JCHAIN*, *CDKN1A*.

Pseudobulk DEA. Pseudobulk analysis was performed using the "bulkDEA" function in the "Seurat_pseudobulk_DEA.R" script in the NUPulmonary/utils repository. Briefly, raw counts (object@assays$RNA@counts) were aggregated by sum by patient and major cell type (e.g., microglia, $CD8^+$ T cells) and passed from Seurat to DESeq2 1.34.0 (86) with relevant metadata. DEA was performed by group, i.e., COVID-19 versus control. Size factor estimation, dispersion fitting, and Wald tests were performed using the DESeq function in DESeq2. "Parametric" and "local" models of dispersion were compared visually for goodness of fit, and the most reasonable fit was chosen. Results were then extracted using the results function with α set to 0.05. Default parameters were used unless otherwise specified. In all plots of pseudobulk gene counts, *P* values shown are FDR-corrected *P* values directly from DESeq2 analysis. For GSEA, the fgsea 1.20.0 package was used (87). Hallmark gene set lists were downloaded from the MSigDB 7.5.1. Enrichment analysis was then performed for all gene sets simultaneously using the "fgseaMultilevel" method using gene-level Wald statistics as rankings and default parameters.

Multiplexed cytokine assays. For in-house assays, cytokine levels in matched BAL fluid and plasma collected from patients were measured using the multiplexed human cytokine/chemokine magnetic bead kits from MilliporeSigma (HCYTMAG-60K-PX41 and HCYP2MAG-62K) according to manufacturer's protocol (HCYTOMAG-60K Rev. 18-MAY-2017). Briefly, frozen BAL and plasma samples were thawed, then spun at 500 rcf for 5 minutes to clarify, and 25 μL of sample was added to 25 μL of premixed magnetic beads in the provided 96-well plate, incubated at 4°C for 4 hours, washed, and sequentially labeled with 25 μL of detection antibodies followed by 25 μL of streptavidin-phycoerythrin prior to analysis using a Luminex 200 system. Raw MFI, bead counts, and standard concentrations were exported and analyzed as described below. Remaining assays were performed by Eve Technologies (Calgary, Alberta, Canada). Samples were thawed and aliquoted at 100 μL, frozen and shipped to the contact research organization on dry ice. The Human Cytokine/Chemokine 71-Plex Discovery Assay (HD71) was then performed on each sample. Custom outputs contained raw MFI values, standard curve concentrations, and bead counts for processing as described below.

Multiplexed cytokine assay processing and analysis. Processing and high-level analysis were performed using custom scripts in R 4.1.1, which are included in the GitHub repository for this publication. Raw MFI values, bead counts, and standard concentrations were first stripped from the data output from either Exponent (in-house assays; Luminex) or bespoke output from Eve Technologies (Calgary, Alberta, Canada). MFI measurements with fewer than 50 bead counts were discarded. Standard curves for each cytokine were then fit for each assay run using self-starting 5-parameter logistic (5PL) models using drc 3.2-0 (88). Cutoffs for curves with low predictive value were then determined empirically using histograms' MFI values versus standard concentrations to identify a bimodal distribution cutoff. For in-house assays, all values calculated using standard curves with MFI < 50 at 100 pg/mL were discarded. For Eve Technologies assays, all values calculated using standard curves with MFI < 50 at 10 pg/mL were discarded. Experimental values for each cytokine were then predicted using the ED function in drc with "absolute" value prediction. In rare cases where a 5PL model could not be hit for an individual cytokine assay combination, these values were excluded (Supplemental Figure 4). Values below the lower asymptote of the model were set to a concentration of 0 pg/mL. Values above the upper asymptote were set to the value of the upper asymptote. Technical replicates (including those across assays) were collapsed by mean with NA values excluded. Analytes showing poor dynamic range were excluded from further analysis. For calculations of cumulative exposure (AUC) by ICU day, a piecewise linear function was first fit for each patient for each analyte for all measurements during the patient's stay using the approxfun function in R stats 4.1.1 using the "linear" method with $n = 100$. Initial measurements were carried out an additional day to represent the time of admission to first measurement, and final measurements were carried out an additional day to represent time until discharge or cessation of measurement. In rare cases where an initial measurement was missing, values were imputed by setting the initial measurement (day = 0) to the first measurement for the analyte/patient pair. Geometric integration was then performed using the integrate function using the day of first measurement as the lower bound and the final day of measurement + 1 as the upper bound. Default parameters were used unless otherwise specified.

Machine learning prediction of COVID-19 status. Initial BAL and plasma samples ($n = 1$/patient) were collected for all patients with a BAL or plasma draw within the first 48 hours of intubation. For healthy control samples, the first sample of each type was used. Data sets were then split 75%/25% train/test at random. A GLM-based logistic regression classification model with binary outcome ("COVID-19" or "Other") was then fit using tidymodels 1.1.0 in R (89, 90).

Bulk cytokine deconvolution. Raw scRNA-Seq counts from Grant et al. (NCBI GEO GSE155249) (33) were imported as an H5AD object using SCANPY 1.9.1 (91). Genes were then filtered to the union between genes detected by scRNA-Seq (counts > 0) and analytes analyzed in multiplexed cytokine assays. Expression of each analyte-encoding gene was then summarized by mean using pandas 1.5.1 (92) and numpy 1.23.4 (93) and exported as a CSV file for further analysis in R 4.1.1 using the environment described herein. For correlations between protein expression by multiplexed cytokine assay and cell type– and cell state–specific scRNA-Seq counts, exact Spearman correlations were performed using cor.test in R stats 4.1.1.

Single-molecule FISH and immunofluorescence. Fixed human postmortem frontal lobe sections were collected as described above and transferred to sterile-filtered 20% sucrose in PBS for 24–48 hours at 4°C until fully equilibrated. This procedure was then repeated with 10% sucrose + 50% Scigen Tissue-Plus O.C.T. Compound (Thermo Fisher Scientific 23-730-571). Equilibrated samples were then embedded in 100% Scigen Tissue-Plus O.C.T. Compound and frozen on dry ice before being stored at –80°C indefinitely. Tissue sectioning and pretreatment were performed according to manufacturer's instructions using the "Fixed-frozen tissue sample preparation and pretreatment" protocol from the RNAScope Multiplex Fluorescent Reagent Kit v2 User manual (ACD 323100-USM/Rev Date: 02272019) and using the RNAscope H_2O_2 and Protease Reagents kit (ACD 322381) and RNA-Protein Co-Detection Ancillary Kit (ACD 323180). Tissues were sectioned using a Cryocut 1800 cryostat (Reichert Jung) at 14 μm. Sections were transferred directly to RT Bond 380 microslides (Matsunami 0380W). Samples were boiled in ACD codetection target retrieval buffer for 5 minutes. All downstream steps were performed according to the RNAscope Multiplex Fluorescent v2 Assay combined with Immunofluorescence - Integrated Co-Detection Workflow (MK 51-150/Rev B/Effective Date: 02/11/2021). For IBA1 staining, sections were stained with an anti-IBA1 antibody at a 1:50 dilution (Abcam ab178847) for 1–2 hours at RT followed by 3 washes in PBS + 0.1% Tween 20 (PBS-T; MilliporeSigma P7949-100ML). Primary antibody was then fixed to the tissue for 30 minutes in 4% paraformaldehyde for 30 minutes at RT followed by 3 washes with PBS-T. Staining by smFISH and mounting were performed as described in the RNAscope 4-plex Ancillary Kit for Multiplex Fluorescent Reagent Kit v2 protocol (ACD 323120-TN/Rev A/Draft Date 12172019) using the RNAscope Multiplex Fluorescent Detection Reagents kit v2 (ACD 323110) and RNAscope 4-Plex Ancillary Kit for Multiplex Fluorescent Kit v2 (ACD 323120). Sections were stained with probes against *CCL2* (channel 1; ACD 423811) conjugated to Opal 690 (Akoya FP1497001KT), *CDKN1A* (channel 2; ACD 311401-C2) conjugated to Opal Polaris 780 (Akoya FP1501001KT), and *IL1B* (channel 4; ACD 310361-C4) conjugated to Opal 620 (Akoya FP1495001KT). Expression of IBA1 was then visualized using a secondary antibody against rabbit IgG conjugated to Alexa Fluor 488 (Life Technologies A21206) at a 1:500 dilution in Co-Detection Antibody Diluent for 30 minutes at RT. Autofluorescence was quenched by treatment with 1× TrueBlack stain (Biotium 23007) in 70% ethanol for 30 seconds followed by 3 washes in PBS. Samples were then counterstained with ACD DAPI solution for 1 minute followed by 1 wash in PBS. Sections were mounted with Prolong Gold mountant (Thermo Fisher Scientific P36930) using VWR No. 1.5 coverglass (VWR 48393-195). Full antibody information is provided in Supplemental Table 3.

RNAscope imaging and image processing. Slides from human brain sections were prepared as described above and imaged with a 60× Plan Apo oil immersion objective (NA 1.4) on a Nikon ECLIPSE Ti2 wide-field inverted microscope equipped with a Photometrics Iris 15 camera at the Northwestern University Center for Advanced Microscopy & Nikon Imaging Center. DAPI, Alexa Fluor 488, Opal 620, Opal 690, and Opal Polaris 780 were captured using a filter set for DAPI (Chroma 49000), EGFP (Chroma 49002), DSRed (Chroma 49005), Cy5 (Chroma 49006), and Cy7 (Nikon 96377), respectively, using LED illumination. *Z*-stacks were acquired for all images shown at 0.3 μm per optical section. Image processing was then performed using a custom macro in FIJI/ImageJ version 2.9.0/1.54b (94, 95). Raw ND2 files were imported using the Bio-Formats plugin without rescaling and split by channel. Each channel was then flattened using a maximum *Z* projection. Background subtraction was then performed individually on each channel using the "Rolling Ball" algorithm individually for each channel using the "Subtract Background" function with a radius of 20 for all RNAScope targets, 50 for DAPI/DNA, and 100 for IBA1. Individual channels were then rescaled with the same LUT. Channels were then merged and pseudocolored using the "Merge Channels" function, converted into an RGB color TIFF, and exported. Individual channels were then inverted and exported as 16-bit TIFFs.

Statistics. Statistical analysis was performed using R 4.1.1 with tidyverse version 1.3.1 (96). For all comparisons, normality was first assessed using a Shapiro-Wilk test and manual examination of distributions. For parameters that exhibited a clear lack of normality, nonparametric tests were used. In cases of multiple

testing, *P* values were corrected using FDR correction. Adjusted *P* values less than 0.05 were considered significant. Two-sided statistical tests were performed in all cases. Plotting was using ggplot 2.3.4.0 unless otherwise noted (97). Heatmaps were generated using ComplexHeatmap 2.10.0 with clustering using Ward's Method (D2) with Euclidean distance as the distance metric (98). Figure layouts were generated using patchwork 1.1.2 and edited in Adobe Illustrator 2023. In all box plots, box limits represent the interquartile range (IQR) with a center line at the median. Whiskers represent the largest point within 1.5× IQR. All points are overlaid. Outlier points are included in these overlaid points but not shown explicitly.

Study approval. All human research was approved by the Northwestern University Institutional Review Board (IRB) and the Duke University IRB. Samples from patients with COVID-19, viral pneumonia, or other pneumonia and from nonpneumonia controls were collected from participants enrolled in SCRIPT study STU00204868. Data from this cohort have been published previously and are available from dbGAP (phs002300.v1.p1) (33, 53, 54). All participants or their legal surrogates provided informed consent. Healthy volunteers were enrolled in the studies Pro00088966 and Pro00100375 at Duke University. Brain autopsy was performed at Northwestern Memorial Hospital, as approved under IRB STU212579 and CSRC-1661.

Data availability. The complete scRNA-Seq data set, including raw FASTQ files, raw and normalized counts, and all relevant metadata, is available through GEO at GSE259276 (https://www.ncbi.nlm.nih.gov/geo/query/acc.cgi?acc=GSE259276). Supporting Data Values are available as an Excel file. An interactive version of Figure 1A with all gene expression data and relevant metadata is available at https://nupulmonary.org/covid-19/human_microglia/?ds=human_microglia_COVID-19.

The complete code used to process data and generate all figures is available at https://github.com/NUPulmonary/2023_Grant_Poor (commit ID 8b56b58). Scripts used for data processing are available at https://github.com/NUPulmonary/utils (commit ID bf1c984).

Author contributions

RAG contributed to experimental design, experiments, data analysis, and the manuscript. TAP contributed to experimental design, experiments, data analysis, sample acquisition, and the manuscript. LS, ED, SS, XGPL, HAV, and ZL contributed to experiments. KJS contributed to the data analysis. JIB, HKD, LMS, and EAO contributed to sample acquisition and data analysis. RMT and JWL contributed to sample acquisition and the manuscript. RGW, BDS, AVM, and GRSB contributed to experimental design, manuscript, and funding. RAG and TAP contributed equally to this work and will list themselves first on their CVs. Order of co–first authorship for publication was determined alphabetically by last name.

Acknowledgments

We would like to thank Constadina Arvanitis in the Northwestern University Center for Advanced Microscopy & Nikon Imaging Center for substantial help with optimization of combined RNAScope and immunofluorescence on human brain samples. The Northwestern University Flow Cytometry Core Facility, Northwestern University Metabolomics Core Facility, and Northwestern University Center for Advanced Microscopy were supported by Cancer Center Support Grant P30 CA060553 awarded to the Robert H. Lurie Comprehensive Cancer Center. We further thank Cara J. Gottardi for her insightful comments on smFISH image presentation and analysis. Finally, we thank the many human participants and their families for their invaluable contributions to this research. The Genomics Compute Cluster is part of Quest, Northwestern University's high-performance computing facility, with the purpose to advance research in genomics. ScRNA-Seq was performed with support from Simpsons Querrey Institute for Epigenetics. Cell sorting was performed on a BD FACSAria SORP cell sorter purchased through the support of NIH 1S10OD011996-01. Additional funding was provided by SQLIFTS at Northwestern University, Dixon Translational Research Grants Initiative, UL1TR001422, Chicago Biomedical Consortium, P01AG049665, P01HL154998, R01HL149883, R01LM013337, R01HL153122, R01HL147290, R01HL147575, R01HL158139, R01ES034350, R01ES027574, I01CX001777, U01TR003528, R21AG075423, T32AG020506, F31AG071225, and T32HL076139. See Supplemental Acknowledgments for details on The NU SCRIPT Investigators.

1. Dong E, et al. An interactive web-based dashboard to track COVID-19 in real time. *Lancet Infect Dis*. 2020;20(5):533–534.
2. Al-Aly Z, et al. High-dimensional characterization of post-acute sequelae of COVID-19. *Nature*. 2021;594(7862):259–264.
3. Taquet M, et al. Neurological and psychiatric risk trajectories after SARS-CoV-2 infection: an analysis of 2-year retrospective

cohort studies including 1 284 437 patients. *Lancet Psychiatry*. 2022;9(10):815–827.
4. Spudich S, Nath A. Nervous system consequences of COVID-19. *Science*. 2022;375(6578):267–269.
5. Nalbandian A, et al. Post-acute COVID-19 syndrome. *Nat Med*. 2021;27(4):601–615.
6. Bailey J, et al. Multidisciplinary center care for long COVID syndrome - a retrospective cohort study [published online May 22, 2023]. *Am J Med*. https://doi.org/10.1016/j.amjmed.2023.05.002.
7. Davydow DS, et al. Functional disability, cognitive impairment, and depression following hospitalization for pneumonia. *Am J Med*. 2013;126(7):615.
8. Shah FA, et al. Bidirectional relationship between cognitive function and pneumonia. *Am J Respir Crit Care Med*. 2013;188(5):586–592.
9. Tate JA, et al. Infection hospitalization increases risk of dementia in the elderly. *Crit Care Med*. 2014;42(5):1037–1046.
10. Global Burden of Disease Long COVID Collaborators, et al. Estimated global proportions of individuals with persistent fatigue, cognitive, and respiratory symptom clusters following symptomatic COVID-19 in 2020 and 2021. *JAMA*. 2022;328(16):1604–1615.
11. Del Brutto OH, et al. Cognitive decline among individuals with history of mild symptomatic SARS-CoV-2 infection: a longitudinal prospective study nested to a population cohort. *Eur J Neurol*. 2021;28(10):3245–3253.
12. Deinhardt-Emmer S, et al. Early postmortem mapping of SARS-CoV-2 RNA in patients with COVID-19 and the correlation with tissue damage. *Elife*. 2021;10:e60361.
13. Fullard JF, et al. Single-nucleus transcriptome analysis of human brain immune response in patients with severe COVID-19. *Genome Med*. 2021;13(1):118.
14. Khan M, et al. Visualizing in deceased COVID-19 patients how SARS-CoV-2 attacks the respiratory and olfactory mucosae but spares the olfactory bulb. *Cell*. 2021;184(24):5932–5949.
15. Taquet M, et al. Acute blood biomarker profiles predict cognitive deficits 6 and 12 months after COVID-19 hospitalization. *Nat Med*. 2023;29(10):2498–2508.
16. Fontes-Dantas FL, et al. SARS-CoV-2 Spike protein induces TLR4-mediated long-term cognitive dysfunction recapitulating post-COVID-19 syndrome in mice. *Cell Rep*. 2023;42(3):112189.
17. Stein SR, et al. SARS-CoV-2 infection and persistence in the human body and brain at autopsy. *Nature*. 2022;612(7941):758–763.
18. Fernández-Castañeda A, et al. Mild respiratory COVID can cause multi-lineage neural cell and myelin dysregulation. *Cell*. 2022;185(14):2452–2468.
19. Chen T, et al. Positive Epstein-Barr virus detection in coronavirus disease 2019 (COVID-19) patients. *Sci Rep*. 2021;11(1):10902.
20. Zhang B-Z, et al. SARS-CoV-2 infects human neural progenitor cells and brain organoids. *Cell Res*. 2020;30(10):928–931.
21. Lucas C, et al. Longitudinal analyses reveal immunological misfiring in severe COVID-19. *Nature*. 2020;584(7821):463–469.
22. Jose RJ, Manuel A. COVID-19 cytokine storm: the interplay between inflammation and coagulation. *Lancet Respir Med*. 2020;8(6):e46–e47.
23. Kuiken T, Taubenberger JK. Pathology of human influenza revisited. *Vaccine*. 2008;26(suppl 4):D59–D66.
24. Levine KS, et al. Virus exposure and neurodegenerative disease risk across national biobanks. *Neuron*. 2023;111(7):1086–1093.
25. Jurgens HA, et al. Influenza infection induces neuroinflammation, alters hippocampal neuron morphology, and impairs cognition in adult mice. *J Neurosci*. 2012;32(12):3958–3968.
26. Hosseini S, et al. Long-term neuroinflammation induced by influenza A virus infection and the impact on hippocampal neuron morphology and function. *J Neurosci*. 2018;38(12):3060–3080.
27. Banks WA, et al. Penetration of interleukin-6 across the murine blood-brain barrier. *Neurosci Lett*. 1994;179(1–2):53–56.
28. Banks WA, et al. Bidirectional transport of interleukin-1 alpha across the blood-brain barrier. *Brain Res Bull*. 1989;23(6):433–437.
29. Gutierrez EG, et al. Murine tumor necrosis factor alpha is transported from blood to brain in the mouse. *J Neuroimmunol*. 1993;47(2):169–176.
30. Henry CJ, et al. Peripheral lipopolysaccharide (LPS) challenge promotes microglial hyperactivity in aged mice that is associated with exaggerated induction of both pro-inflammatory IL-1beta and anti-inflammatory IL-10 cytokines. *Brain Behav Immun*. 2009;23(3):309–317.
31. Cosentino G, et al. Neuropathological findings from COVID-19 patients with neurological symptoms argue against a direct brain invasion of SARS-CoV-2: a critical systematic review. *Eur J Neurol*. 2021;28(11):3856–3865.
32. Soung AL, et al. COVID-19 induces CNS cytokine expression and loss of hippocampal neurogenesis. *Brain*. 2022;145(12):4193–4201.
33. Grant RA, et al. Circuits between infected macrophages and T cells in SARS-CoV-2 pneumonia. *Nature*. 2021;590(7847):635–641.
34. Alonso-Lana S, et al. Cognitive and neuropsychiatric manifestations of COVID-19 and effects on elderly individuals with dementia. *Front Aging Neurosci*. 2020;12:588872.
35. Ho C-Y, et al. Postmortem assessment of olfactory tissue degeneration and microvasculopathy in patients with COVID-19. *JAMA Neurol*. 2022;79(6):544–553.
36. Mosher KI, Wyss-Coray T. Microglial dysfunction in brain aging and Alzheimer's disease. *Biochem Pharmacol*. 2014;88(4):594–604.
37. Landel V, et al. Temporal gene profiling of the 5XFAD transgenic mouse model highlights the importance of microglial activation in Alzheimer's disease. *Mol Neurodegener*. 2014;9(1):33.
38. Keren-Shaul H, et al. A unique microglia type associated with restricting development of Alzheimer's disease. *Cell*. 2017;169(7):1276–1290.
39. Gulen MF, et al. cGAS–STING drives ageing-related inflammation and neurodegeneration. *Nature*. 2023;620(7973):374–380.
40. Braak H, Braak E. Neuropathological stageing of Alzheimer-related changes. *Acta Neuropathol*. 1991;82(4):239–259.
41. Olah M, et al. Single cell RNA sequencing of human microglia uncovers a subset associated with Alzheimer's disease. *Nat Commun*. 2020;11(1):6129.
42. Budinger GRS, et al. Distinctive features of severe SARS-CoV-2 pneumonia. *J Clin Invest*. 2021;131(14):e149412.
43. Nin N, et al. Clinical characteristics and outcomes of patients with 2009 influenza A(H1N1) virus infection with respiratory failure requiring mechanical ventilation. *J Crit Care*. 2011;26(2):186–192.
44. Hong SB, et al. Epidemiological analysis of critically ill adult patients with pandemic influenza A(H1N1) in South Korea. *Epidemiol Infect*. 2013;141(5):1070–1079.

45. Li Q, et al. Early transmission dynamics in Wuhan, China, of novel coronavirus-infected pneumonia. *N Engl J Med*. 2020;382(13):1199–1207.
46. Grasselli G, et al. Baseline characteristics and outcomes of 1591 patients infected with SARS-CoV-2 admitted to ICUs of the Lombardy region, Italy. *JAMA*. 2020;323(16):1574–1581.
47. Huang C, et al. Clinical features of patients infected with 2019 novel coronavirus in Wuhan, China. *Lancet*. 2020;395(10223):497–506.
48. Kim D, et al. The architecture of SARS-CoV-2 transcriptome. *Cell*. 2020;181(4):914–921.
49. Gold JE, et al. Investigation of long COVID prevalence and its relationship to Epstein-Barr virus reactivation. *Pathogens*. 2021;10(6):763.
50. Paolicelli RC, et al. Microglia states and nomenclature: a field at its crossroads. *Neuron*. 2022;110(21):3458–3483.
51. Safaiyan S, et al. White matter aging drives microglial diversity. *Neuron*. 2021;109(7):1100–1117.
52. Liberzon A, et al. Molecular Signatures Database (MSigDB) 3.0. *Bioinformatics*. 2011;27(12):1739–1740.
53. Gao CA, et al. Machine learning links unresolving secondary pneumonia to mortality in patients with severe pneumonia, including COVID-19. *J Clin Invest*. 2023;133(12):e170682.
54. Markov N, et al. SCRIPT CarpeDiem Dataset: demographics, outcomes, and per-day clinical parameters for critically ill patients with suspected pneumonia. *PhysioNet*. 2000;101(23):e215–e220.
55. Zhang F, et al. IFN-γ and TNF-α drive a *CXCL10+ CCL2+* macrophage phenotype expanded in severe COVID-19 lungs and inflammatory diseases with tissue inflammation. *Genome Med*. 2021;13:64.
56. Roussel M, et al. Comparative immune profiling of acute respiratory distress syndrome patients with or without SARS-CoV-2 infection. *Cell Rep Med*. 2021;2(6):100291.
57. Flament H, et al. Outcome of SARS-CoV-2 infection is linked to MAIT cell activation and cytotoxicity. *Nat Immunol*. 2021;22(3):322–335.
58. Wendisch D, et al. SARS-CoV-2 infection triggers profibrotic macrophage responses and lung fibrosis. *Cell*. 2021;184(26):6243–6261.
59. RECOVERY Collaborative Group, et al. Dexamethasone in hospitalized patients with Covid-19 - preliminary report. *N Engl J Med*. 2021;384(8):693–704.
60. Rennard SI, et al. Estimation of volume of epithelial lining fluid recovered by lavage using urea as marker of dilution. *J Appl Physiol (1985)*. 1986;60(2):532–538.
61. Hönzke K, et al. Human lungs show limited permissiveness for SARS-CoV-2 due to scarce ACE2 levels but virus-induced expansion of inflammatory macrophages. *Eur Respir J*. 2022;60(6):2102725.
62. Thakur KT, et al. Neurological issues in children with COVID-19. *Neurosci Lett*. 2021;743:135567.
63. Delorey TM, et al. COVID-19 tissue atlases reveal SARS-CoV-2 pathology and cellular targets. *Nature*. 2021;595(7865):107–113.
64. Richwine AF, et al. Architectural changes to CA1 pyramidal neurons in adult and aged mice after peripheral immune stimulation. *Psychoneuroendocrinology*. 2008;33(10):1369–1377.
65. Münch G, et al. Microglial activation induces cell death, inhibits neurite outgrowth and causes neurite retraction of differentiated neuroblastoma cells. *Exp Brain Res*. 2003;150(1):1–8.
66. Neumann H, et al. Tumor necrosis factor inhibits neurite outgrowth and branching of hippocampal neurons by a rho-dependent mechanism. *J Neurosci*. 2002;22(3):854–862.
67. Kox M, et al. Cytokine levels in critically ill patients with COVID-19 and other conditions. *JAMA*. 2020;324(15):1565–1567.
68. Vijayakumar B, et al. Immuno-proteomic profiling reveals aberrant immune cell regulation in the airways of individuals with ongoing post-COVID-19 respiratory disease. *Immunity*. 2022;55(3):542–556.
69. Lansbury L, et al. Corticosteroids as adjunctive therapy in the treatment of influenza. *Cochrane Database Syst Rev*. 2019;2:CD010406.
70. Eltzschig HK, Carmeliet P. Hypoxia and inflammation. *N Engl J Med*. 2011;364(7):656–665.
71. Cummins EP, et al. Prolyl hydroxylase-1 negatively regulates IkappaB kinase-beta, giving insight into hypoxia-induced NFkappaB activity. *Proc Natl Acad Sci U S A*. 2006;103(48):18154–18159.
72. Walmsley SR, et al. Hypoxia-induced neutrophil survival is mediated by HIF-1alpha-dependent NF-kappaB activity. *J Exp Med*. 2005;201(1):105–115.
73. Lee MH, et al. Neurovascular injury with complement activation and inflammation in COVID-19. *Brain*. 2022;145(7):2555–2568.
74. Balczon R, et al. Pneumonia initiates a tauopathy. *FASEB J*. 2021;35(9):e21807.
75. Balczon R, et al. Lung endothelium, tau, and amyloids in health and disease. *Physiol Rev*. 2024;104(2):533–587.
76. Hippensteel JA, et al. Circulating heparan sulfate fragments mediate septic cognitive dysfunction. *J Clin Invest*. 2019;129(4):1779–1784.
77. Walter JM, et al. Multidimensional assessment of alveolar T cells in critically ill patients. *JCI Insight*. 2018;3(17):e123287.
78. Pickens CI, et al. An adjudication protocol for severe pneumonia. *Open Forum Infect Dis*. 2023;10(7):ofad336.
79. Wolock SL, et al. Scrublet: computational identification of cell doublets in single-cell transcriptomic data. *Cell Syst*. 2019;8(4):281–291.
80. Fleming SJ, et al. Unsupervised removal of systematic background noise from droplet-based single-cell experiments using CellBender. *Nat Methods*. 2023;20(9):1323–1335.
81. Satija R, et al. Spatial reconstruction of single-cell gene expression data. *Nat Biotechnol*. 2015;33(5):495–502.
82. Lopez R, et al. Deep generative modeling for single-cell transcriptomics. *Nat Methods*. 2018;15(12):1053–1058.
83. Mangiola S, et al. Interfacing Seurat with the R tidy universe. *Bioinformatics*. 2021;37(22):4100–4107.
84. Hafemeister C, Satija R. Normalization and variance stabilization of single-cell RNA-seq data using regularized negative binomial regression. *Genome Biol*. 2019;20(1):296.
85. Traag VA, et al. From Louvain to Leiden: guaranteeing well-connected communities. *Sci Rep*. 2019;9(1):5233.
86. Love MI, et al. Moderated estimation of fold change and dispersion for RNA-seq data with DESeq2. *Genome Biol*. 2014;15(12):550.
87. Korotkevich G, et al. Fast gene set enrichment analysis [preprint]. https://doi.org/10.1101/060012. Posted on bioRxiv February 1, 2021.

88. Ritz C, et al. Dose-response analysis using R. *PLoS One*. 2015;10(12):e0146021.
89. Kuhn M, Wickham H. Tidymodels: a collection of packages for modeling and machine learning using tidyverse principles. https://www.tidymodels.org/. Updated 2020. Accessed March 21, 2024.
90. Kuhn M, Johnson K, eds. *Applied Predictive Modeling*. Springer New York; 2013.
91. Wolf FA, et al. SCANPY: large-scale single-cell gene expression data analysis. *Genome Biol*. 2018;19(1):15.
92. McKinney W. pandas: a Foundational Python Library for Data Analysis and Statistics. https://www.dlr.de/sc/en/Portaldata/15/Resources/dokumente/pyhpc2011/submissions/pyhpc2011_submission_9.pdf. Updated 2011. Accessed March 21, 2024.
93. Van der Walt S, et al. The NumPy array: a structure for efficient numerical computation. *Comput Sci Eng*. 2011;13(2):22–30.
94. Abràmoff MD, et al. Image Processing with ImageJ. https://imagescience.org/meijering/publications/download/bio2004.pdf Updated 2004. Accessed March 21, 2024.
95. Schindelin J, et al. Fiji: an open-source platform for biological-image analysis. *Nat Methods*. 2012;9(7):676–682.
96. Wickham H, et al. Welcome to the Tidyverse. *J Open Source Softw*. 2019;4(43):1686.
97. Wickham H, ed. *ggplot2: Elegant Graphics for Data Analysis*. Springer; 2016.
98. Gu Z, et al. Complex heatmaps reveal patterns and correlations in multidimensional genomic data. *Bioinformatics*. 2016;32(18):2847–2849.